

Observation of Erratic Non-Hermitian Skin Localization and Transport

Jia-Xin Zhong^{1,2}, Jee Woo Kim², Stefano Longhi^{3,4,*}, and Yun Jing^{2,†}

¹Key Laboratory of Modern Acoustics and Institute of Acoustics, Nanjing University, Nanjing 210093, China

²Graduate Program in Acoustics, The Pennsylvania State University, University Park, PA 16802, USA

³Dipartimento di Fisica, Politecnico di Milano, Piazza Leonardo da Vinci 32, I-20133 Milano, Italy

⁴IFISC (UIB-CSIC), Instituto de Fisica Interdisciplinaria Sistemas Complejos, E-07122 Palma de Mallorca, Spain

*stefano.longhi@polimi.it; †yqj5201@psu.edu

Abstract

Localization is a pervasive phenomenon across physics, shaping transport from electrons in solids to light and sound in engineered media. In traditional settings, disorder strongly impedes transport, resulting in dynamical localization or, at best, sub-ballistic or diffusive dynamics. A distinct and previously unobserved regime, erratic non-Hermitian skin localization (ENHSL), can arise in globally reciprocal non-Hermitian lattices with disorder. It features macroscopic, disorder-dependent localization at irregular bulk positions with subexponential decay, linked to stochastic interfaces governed by the universal order statistics of random walks. We realize this regime experimentally in an acoustic lattice implementing a disordered Hatano-Nelson chain with imaginary gauge fields. Using Green's-function-based spectroscopy together with time-resolved measurements on the same platform, we reconstruct the full complex spectrum and eigenstates, and directly observe wave-packet dynamics. Remarkably, we observe ballistic transport despite strong spectral localization. We develop a transport theory that connects the dominant propagation site to the maximal random-walk excursion within an expanding light cone and predicts a universal Lévy-arc sine statistics, in quantitative agreement with experiment. Our results decouple eigenstate localization from transport and establish ENHSL as a new paradigm for wave dynamics.

Introduction

Wave localization is a unifying phenomenon across physics, shaping transport in systems ranging from electrons in solids to light, sound, and other engineered media. The most celebrated example, Anderson localization [1–3], arises when disorder disrupts an underlying periodic structure, producing exponentially localized eigenstates and strongly inhibited motion. Even in special models where the localization length becomes unbounded, transport remains at most sub-ballistic [4–6], and transitions to extended phases proceed via mobility edges through critical, fractal states [3, 7].

Non-Hermitian systems [8]—featuring gain, loss, or effective non-reciprocal couplings—have recently expanded the landscape of localization and transport phenomena. A paradigmatic example is the non-Hermitian skin effect (NHSE) in disorder-free lattices [9–22] where asymmetric couplings cause an extensive set of bulk modes to accumulate at system boundaries, overturning conventional bulk-boundary correspondence. In disordered non-Hermitian systems, Anderson localization also arises [23–30] yet, unlike in Hermitian settings, wave propagation can persist even when all eigenstates remain exponentially localized with a bounded localization length. This counterintuitive transport is driven by the stochastic lifetimes of localized modes [30–34] generating jump-like dynamics [30, 32–34] and universal sub-ballistic spreading [33].

Despite these differences, Anderson localization in both Hermitian and non-Hermitian systems is traditionally characterized by two shared hallmarks: exponentially localized eigenstates with spatial profiles dictated by disorder and stochastically centered throughout the system; and a corresponding suppression of ballistic transport, yielding either dynamical localization, diffusive or sub-ballistic motion. These features have long shaped our intuition about the interplay between disorder and wave propagation.

Here we experimentally demonstrate a fundamentally different localization regime—erratic non-Hermitian skin localization (ENHSL)—that emerges in globally reciprocal non-Hermitian lattices with disorder [35]. Unlike Anderson localization or the NHSE, ENHSL produces macroscopic and highly irregular localization peaks whose positions vary unpredictably across disorder realizations. The resulting spatial profiles display subexponential decay, are not fractal, and reflect stochastic interfaces governed by the order statistics of a symmetric random walk [35], establishing a direct link between non-Hermitian disorder and universal stochastic processes.

Realizing this phenomenon experimentally is technically challenging because it requires a platform with tunable non-Hermitian couplings, controllable disorder over many realizations, and global reciprocity, together with the direct access to both spectral observables (complex eigenvalues and eigenstates) and time-resolved propagation. Active acoustic lattices meet these requirements, offering tunable non-Hermitian couplings via pump-probe feedback, flexible disorder implementation, and high-accuracy wave field measurements [36–41]. Building on our

Green's-function-based spectroscopy technique for reconstructing the full complex spectrum and eigenstates [41], we further develop time-resolved measurements to track wave-packet dynamics, enabling a unified spectral-and-dynamical characterization of erratic localization and transport on the same platform. Using this platform to implement a disordered Hatano–Nelson model with imaginary gauge fields, we directly observe the defining signatures of ENHSL: large-scale, sample-specific bulk localization peaks with strongly fluctuating positions across disorder realizations. Beyond establishing the spectral signatures of ENHSL, we develop and experimentally validate a complementary theory for wave-packet dynamics and transport that extends the original spectral picture of ENHSL. Our measurements reveal that, despite strong spectral localization, the ensemble-averaged spreading remains ballistic.

Specifically, we find that wave excitations are drawn toward the site where the symmetric random-walk landscape attains its largest excursion within the light cone of the disorder-free lattice. This dominant site is a stochastic, time-dependent quantity whose distribution follows the universal Lévy arcsine law. This mechanism reveals that strong non-Hermitian localization does not necessarily impede ballistic motion—contradicting the long-standing assumption that disorder-induced confinement must inhibit transport or reduce it to sub-ballistic or diffusive behaviour.

Results

Model and conceptual overview

We consider a one-dimensional (1D) Hatano–Nelson chain [23] with spatially disordered imaginary gauge fields h_n [35, 42], sketched in Fig. 1a. The defining feature is that local non-reciprocity fluctuates from link to link, yet the net imaginary gauge bias vanishes in each realization, i.e. $\sum_n h_n = 0$ (global reciprocity). In the tight-binding description, the right/left hoppings on link n are

$$J_n^R = J e^{h_n}, \quad J_n^L = J e^{-h_n}, \quad (1)$$

where $\{h_n\}$ are independent random variables drawn from a distribution $f(h)$ with zero mean. In this work, we sample h_n from a uniform distribution $h_n \sim \mathcal{U}(-\Delta h, \Delta h)$, while the key dynamical predictions depend only on the symmetry and finite variance of $f(h)$. A convenient way to represent the gauge disorder is via the cumulative gauge field (random-walk landscape)

$$X_n = \sum_{\ell=0}^{n-1} h_\ell, \quad (2)$$

which maps the link disorder to a symmetric random walk in the site coordinate n . According to the spectral theory of the ENHSL [35], large excursions of X_n give rise to stochastic interfaces that seed macroscopic localization structures through local skin localization. This leads to the

natural question of whether the spectral localization inherent to the ENHSL permits any form of transport, or instead fully suppresses it. Although spectral localization is typically linked to dynamical localization or sub-ballistic transport [4–6, 30–33], we show here that the extremal statistics of X_n can, quite unexpectedly, enable on average ballistic transport.

To emphasize the genuinely new features of ENHSL, Fig. 1 compares this globally reciprocal non-Hermitian model (Fig. 1a) with a conventional Hermitian (Anderson) disordered chain (Fig. 1b). In the globally reciprocal disordered Hatano-Nelson chain, ENHSL appears in each realization as macroscopic localization peaks at irregular *bulk* positions, with all eigenstates displaying sub-exponential localization. A schematic eigenstate profile is shown in Fig. 1c: a dominant bulk peak is typically accompanied by a few weaker satellite peaks, producing a strongly nonuniform mode-summed intensity $\Psi_n = \sum_m |\psi_{m,n}|^2$, which is itself dominated by the same peak structure. Here, $\psi_{m,n}$ is the amplitude of the m th (right) eigenstate at site n and normalized such that $\sum_n |\psi_{m,n}|^2 = 1$. A second defining spectral property is that the spectrum is real, and remains essentially insensitive to boundary conditions: switching between open (OBC) and periodic (PBC) boundary conditions does not induce the qualitative spectral reshaping characteristic of the conventional NHSE. For comparison, Fig. 1d sketches the Anderson-localized situation.

A major finding is that the dynamical response provides the sharpest contrast between ENHSL and Anderson localization. Figure 1e illustrates the ENHSL dynamics following a bulk-centered excitation. In a single disorder realization (3D traces), the wave packet does not simply spread and then freeze, nor does it become pinned to a static defect-like site. Instead, the dynamics is dominated by an attraction toward a realization-dependent bulk region associated with the dominant excursion of the random-walk landscape X_n within the finite-time light cone of the underlying disorder-free chain. Accordingly, the wave-packet develops a pronounced peak that is strong, macroscopic, and highly sample specific. Most importantly, ENHSL exhibits an ensemble-level transport behavior that is counterintuitive from the viewpoint of conventional disorder physics. The ensemble statistics reveal that the spreading distance can remain ballistic on average, which is schematically indicated in Fig. 1e. In other words, ENHSL fully decouples spectral eigenstate localization from transport suppression, allowing ballistic spreading on average. Figure 1f summarizes the Anderson-localized dynamical benchmark, where the wave packet becomes dynamically localized. Ensemble averaging does not restore ballistic motion; instead, it further reinforces the picture of inhibited transport typical of Anderson localization.

Unified spectral-and-dynamical measurement protocol

In this work, we experimentally realize the globally reciprocal Hatano-Nelson model in an engineered acoustic lattice platform [36–41]. Spatial disorder is introduced in a controlled manner by implementing the link asymmetry according to a prescribed sequence $\{h_n\}$. Different

disorder realizations are generated by setting distinct sequences $\{h_n\}$, implemented through calibrated gain and phase settings in the amplifiers and phase shifters (see Methods). We implement a unified spectral-and-dynamical protocol on the same acoustic lattice (Fig. 2a). In the spectral measurements, we perform site-by-site excitation (pump at site j) while recording the steady-state responses at all sites (probe at site i), thereby obtaining the frequency-resolved Green's-function matrix $G_{ij}(\omega)$ (Fig. 2b). By diagonalizing the full measured Green's function matrix (Fig. 2c), we obtain the complete complex spectrum $\{E_m\}$ and corresponding eigenstates $\{\psi_{m,n}\}$, which further enable the evaluation of mode-resolved quantities such as the inverse participation ratio (IPR) and mode-summed intensity Ψ_n (see [41] for details).

In the dynamical measurements, we excite the lattice with a Gaussian-modulated tone burst $s(t)$ centered at frequency $\text{Re}(\omega_0)$ (Fig. 2d)

$$s(t) = \exp \left[-\frac{(t - t_0)^2}{2\sigma^2} - i \text{Re}(\omega_0)t \right]. \quad (3)$$

Here, t_0 is the pulse center time, and ω_0 is the complex resonant frequency of a single cavity with the imaginary part accounting for intrinsic losses. The pulse width σ is chosen to satisfy two experimental constraints: (i) σ cannot be too small, otherwise the injected energy becomes insufficient and the propagating wave packet rapidly decays into the noise floor; (ii) σ cannot be too large, otherwise the excitation spectrum becomes too narrow to cover the relevant bandwidth of the lattice spectrum (Fig. 2e,f). The time-resolved signals are simultaneously recorded at all sites using synchronized data acquisition modules. Importantly, the envelope of these time-domain measurements are extracted to represent the wavefunctions $\psi_n(t)$ (see Methods).

Experimental observation of ENHSL spectral signatures

We first experimentally observe the spectral features of ENHSL under both PBC and OBC. Figures 3a,b compare experimental and tight-binding simulated spectra for a representative realization, showing good agreement. Despite locally non-reciprocal hoppings, the spectrum remains nearly real up to an overall uniform loss shift (-6 Hz) for both PBC and OBC. Figures 3c,d show the spatial distributions of the eigenstates $|\psi_{m,n}|$, with the random-walk landscape X_n overlaid (right axis). ENHSL manifests as macroscopic localization peaks whose positions correlate with large excursions of X_n , and which persist and are only weakly modified when switching between PBC and OBC. This weak boundary sensitivity contrasts sharply with the conventional NHSE in clean non-reciprocal lattices, where switching boundary conditions qualitatively reshapes both spectrum and localization [41]. From Figs. 3b and 3d, we see that all eigenstates have the same IPR under PBC, whereas under OBC a small subset of states shows noticeable deviations. Nevertheless, all eigenstates remain strongly localized under both boundary conditions.

To quantify the system-size dependence, we performed experiments for varying lattice size $N = 5$ to $N = 70$ with a step 5 under OBC. For each lattice size, we measured $R = 8$ disorder realizations (see Supplementary Materials for representative realizations). For each realization, we compute the mode-averaged IPR, $\overline{\text{IPR}}_r = N^{-1} \sum_{m=1}^N \text{IPR}_m$, and then average over realizations to obtain $\langle \text{IPR} \rangle = R^{-1} \sum_{r=1}^R \overline{\text{IPR}}_r$. Figure 3e presents the averaged IPR versus chain length N , compared between experiment and simulation showing good agreement. We characterize the size scaling by fitting $\langle \text{IPR} \rangle \propto N^{-\beta}$, where β is an effective scaling exponent. For extended and localized states, β takes the values 1 and 0, respectively, while $0 < \beta < 1$ indicates fractal states. As shown in Fig. 3e, $\ln \langle \text{IPR} \rangle$ is approximately independent of $\ln N$, yielding $\beta \simeq 0$. This experimental observation confirms the strong spectral localization of eigenstates in ENHSL, although the localization is sub-exponential due to the vanishing of the Lyapunov exponent [35].

Theoretical description of ENHSL dynamics

The spectral formulation of ENHSL describes eigenstate localization via the random-walk landscape X_n induced by the stochastic imaginary gauge field. Here, we present a complementary dynamical perspective. To reveal the single-particle dynamics, we apply the non-unitary gauge transformation $\psi_n(t) = \phi_n(t) \exp(X_n)$, which maps the system onto a uniform Hermitian nearest-neighbor chain with hopping J . For a single-site initial excitation at $n = 0$, the Hermitian solution is given by $\phi_n(t) = (-i)^n J_n(2Jt)$, where $J_n(\cdot)$ is the Bessel function of first kind. Transforming back to the original variables, the normalized occupation probability profile at site n and time t is

$$P_n(t) = \frac{|\psi_n(t)|^2}{\sum_{n'} |\psi_{n'}(t)|^2} = \frac{J_n^2(2Jt) \exp(2X_n)}{\sum_{n'} J_{n'}^2(2Jt) \exp(2X_{n'})}. \quad (4)$$

We quantify transport in a single realization using the second moment $d(t) = \sqrt{\sum_n n^2 P_n(t)}$. In the disorder-free limit $h_n = 0$ (hence $X_n = 0$), one recovers ballistic spreading $d(t) = \sqrt{2} Jt$. Therefore, the disorder-free ballistic spreading is retained in the underlying propagator, while the stochastic gauge factors reshape where intensity accumulates. As a result, the finite-time intensity profile can be viewed as a Hermitian ballistic core modulated by an envelope $\exp(2X_n)$, which locally amplifies ($X_n > 0$) or suppresses ($X_n < 0$) intensity.

At finite time t , the Bessel kernel confines the dynamics with a super-exponential localization to a light-cone-like accessible interval $|n| \lesssim n_{\text{LB}}(t)$, with a linear-in-time Lieb-Robinson (LB) bound $n_{\text{LB}}(t) \simeq 2Jt$. Within this interval, ENHSL dynamics is controlled by an extremal statistic: the wave packet is predominantly localized around the dominant site $n_0(t) = \arg \max_n P_n(t)$, which follows the location where X_n attains its largest excursion within the light cone. This dominant-site picture is crucial: the dynamics is governed by the maximum excursion of a symmetric random walk over an expanding interval, rather than by typ-

ical disorder fluctuations. As X_n is a symmetric random walk, the position of its maximum over a finite interval exhibits a universal limiting distribution according to the Sparre–Anderson theorem [43–46]. Consequently, for sufficiently large t the empirical distribution of $n_0(t)$ approaches the Lévy–arcsine law mapped to the interval $[-n_{\text{LB}}(t), n_{\text{LB}}(t)]$ (derivation in Methods),

$$P_{\text{arc}}(n_0, t) = \frac{1}{\pi \sqrt{[n_{\text{LB}}(t) - n_0][n_0 + n_{\text{LB}}(t)]}}, \quad |n_0| < n_{\text{LB}}(t). \quad (5)$$

Equation (5) predicts an enhanced probability of finding the dominant site near the light-cone edges, $|n_0| \sim n_{\text{LB}}(t)$. Furthermore, by using Eq. (5), the second moment averaged over all locations can be approximated as $\langle d(t) \rangle \simeq \sqrt{\sum_n n^2 P_{\text{arc}}(n_0 = n, t)} = \sqrt{2} Jt$, which clearly shows the ballistic scaling.

Experimental observation of single-realization dynamics

Guided by the dynamical theory, we first experimentally observe the extremal-selection mechanism at the level of individual disorder realizations. Figures 4a–c presents three representative realizations for ENHSL dynamics (see Supplementary Materials for more realizations), compared with two reference cases: (Fig. 4d) clean Hermitian chain (ballistic spreading benchmark) and (Fig. 4e) a disordered Hermitian chain (Anderson localization benchmark). For each ENHSL realization (Fig. 4a–c), the mode-summed eigenstate intensity $\Psi_n = \sum_m |\psi_{m,n}|^2$ exhibits a prominent macroscopic peak (often accompanied by a few weaker satellite peaks). This peak structure is fundamentally different from the Anderson reference (Fig. 4e), where the sum over many exponentially localized eigenstates with random centers yields a comparatively featureless Ψ_n . In ENHSL, the random-walk profile X_n shown in the second row of each panel acts as the organizing structure: prominent spectral peaks emerge near its large excursions, consistent with the spectral picture.

The third row of Fig. 4 shows the measured spatiotemporal evolution $|\psi_n(t)|$ following excitation at the central site. The corresponding simulation results are presented in the fourth row, showing good agreement with experiment for all configurations. In each ENHSL realization, $|\psi_n(t)|$ develops a pronounced localization peak at an irregular bulk position, in agreement with the theoretical picture that dynamics is drawn toward a dominant excursion of X_n . Importantly, this localization peak does not simply coincide with a fixed Anderson-like center; rather, the region of maximal intensity is selected by the disorder realization and can evolve in time within the expanding light cone interval. In several realizations, the dominant intensity ridge in the (n, t) plane reveals a slow drift of the peak position as time increases, reflecting the fact that $n_0(t)$ is defined by an extremal statistic on an expanding interval $(-n_{\text{LB}}(t), n_{\text{LB}}(t))$. In contrast, the Hermitian disorder-free reference (Fig. 4d) exhibits the ballistic spreading pattern, while the Anderson reference (Fig. 4e) shows rapid confinement of $|\psi_n(t)|$ near the initial excitation site,

consistent with dynamical localization.

To quantify spreading, we extract a spreading distance $d(t)$ from $|\psi_n(t)|$ and compare experiment and tight-binding simulations (bottom row of Fig. 4). For ENHSL realizations, $d(t)$ can grow fast and saturate slowly (Fig. 4a) or grow slower than the ballistic reference (Fig. 4c), or exhibit intermediate behaviours (Fig. 4b). These representative realizations show distinct evolution patterns for ENHSL depending on the disorder realization, reflecting strong sample-to-sample fluctuations. For reference, the clean Hermitian chain (Fig. 4d) shows $d(t)$ growing almost linearly with time, while the Anderson reference (Fig. 4e) shows $d(t)$ saturating quickly.

Experimental observation of ensemble dynamics and Lévy-arc sine law

We now turn from representative realizations to ensemble-level transport and statistics. Figure 5a shows the ensemble-averaged ($R = 100$ realizations) spreading distance $\langle d(t) \rangle$ extracted from the measured wave packets and compared with tight-binding simulations. The ENHSL data exhibit a robust linear growth over the experimentally accessible time window, consistent with ballistic transport. For comparison, the clean Hermitian chain shows the ballistic scaling, whereas the Anderson-localized reference saturates, reflecting conventional dynamical localization.

Beyond the mean, Figs. 5b–e present the distributions of $d(t)$ at several fixed times. To faithfully estimate the probability density from a finite ensemble without boundary artefacts, we employ a bounded kernel density estimation (KDE) on the finite support of d (caption of Fig. 5). These panels visualize two important aspects of ENHSL dynamics. First, the distributions are broad and strongly time dependent, reflecting significant realization-to-realization fluctuations. This broadness is expected because the dynamics is governed by extremal statistics of the random walk X_n , which naturally produces large sample-to-sample variability. Second, the weight of the distribution shifts to larger d as time increases, consistent with the expansion of the accessible light-cone interval. In contrast, the Anderson reference would exhibit distributions that rapidly narrow and remain confined, consistent with saturation of $d(t)$.

While $d(t)$ provides a natural bulk measure of spreading, the most discriminating test of the dynamics theory concerns the dominant-site statistics. For each realization, we extract $n_0(t) = \arg \max_n |\psi_n(t)|$, and obtain its distribution $P(n_0, t)$. The theory predicts that $n_0(t)$ follows the Lévy–arc sine law on the finite interval $(-n_{\text{LB}}(t), n_{\text{LB}}(t))$, Eq. (5), where the bound $n_{\text{LB}}(t) = 2Jt$ is fixed by the independently known coupling J . Figure 5f shows the measured $P(n_0, t)$ at $t = 0.5$ s (correspondingly, $n_{\text{LB}} = 25$) and compares it with both simulation and the arcsine prediction. The measured distribution is strongly nonuniform and enhanced toward the edges of the accessible interval, as expected from the arcsine law. This agreement constitutes a stringent verification because it tests the full functional form rather than just a scaling trend, and hinges on an extremal statistic that is explicitly connected to the underlying random walk.

The arcsine-law verification also provides an explanation for ballistic ensemble transport. A symmetric random walk attains its maximum near the boundaries of a finite interval with high probability, and therefore the typical magnitude of the maximizer scales as $|n_0| \sim n_{LB}(t)$. Since $n_{LB}(t) \propto t$, the typical displacement associated with the dominant peak grows linearly, yielding ballistic scaling for $\langle d(t) \rangle$ even though each realization appears localized at any fixed time.

Discussions

Our results provide the first experimental demonstration of a fundamentally new localization regime in non-Hermitian systems, in which strong, macroscopic localization robustly coexists with ballistic transport. Distinct from both Hermitian Anderson localization—where spectral localization is inseparable from dynamical arrest—and from the conventional NHSE—where bulk modes accumulate exponentially at boundaries—ENHSL establishes a fundamentally different paradigm: globally reciprocal non-Hermiticity and disorder jointly generate realization-dependent bulk localization peaks with subexponential profiles, while the associated wave-packet dynamics remains transport preserving on average. A central outcome of our work is the identification and verification of an extremal-statistics mechanism for transport. By combining full spectral reconstruction with time-resolved measurements on the same platform, we directly connect the dominant propagation site to the largest excursion of a symmetric random-walk landscape within a finite-time light cone, and we confirm the resulting universal Lévy-arcsine statistics. Beyond identifying a new form of wave localization, our findings open new directions in the study of complex wave dynamics and reveal a broadly applicable mechanism relevant to quantum and classical waves alike—from condensed matter and photonics to acoustics, metamaterials and other complex media. More generally, ENHSL highlights a route toward engineering stochastic yet controllable wave confinement with predictable ensemble transport, and it motivates future studies of how extremal statistics, topology, interactions, or higher dimensions reshape the relation between localization and propagation in complex non-Hermitian systems.

Acknowledgment

Y. J. thanks the support of startup funds from Penn State University and NSF CMMI awards 2039463 and 195122.

Author contributions

J.-X. Z., S. L., and Y. J. conceived the project. S. L. and J.-X. Z. performed theoretical analysis and numerical simulations. J.-X. Z. designed and performed the experiments with assistance

from J. W. K.. J.-X. Z., S. L., and Y. J. wrote the paper. S. L. and Y. J. supervised the project.

Competing interests

The authors declare no competing interests.

References

- [1] P. W. Anderson. Absence of diffusion in certain random lattices. *Phys. Rev.*, 109(5):1492–1505, March 1958.
- [2] D. J. Thouless. Electrons in disordered systems and the theory of localization. *Phys. Rep.*, 13(3):93–142, October 1974.
- [3] Ferdinand Evers and Alexander D. Mirlin. Anderson transitions. *Rev. Mod. Phys.*, 80(4):1355–1417, October 2008.
- [4] R. del Rio, S. Jitomirskaya, Y. Last, and B. Simon. What is Localization? *Phys. Rev. Lett.*, 75(1):117–119, July 1995.
- [5] David H. Dunlap, H-L. Wu, and Philip W. Phillips. Absence of localization in a random-dimer model. *Phys. Rev. Lett.*, 65(1):88–91, July 1990.
- [6] H.-L. Wu and Philip Phillips. Polyaniline is a random-dimer model: A new transport mechanism for conducting polymers. *Phys. Rev. Lett.*, 66(10):1366–1369, March 1991.
- [7] H. Aoki. Critical behaviour of extended states in disordered systems. *J. Phys. C: Solid State Phys.*, 16(6):L205, February 1983.
- [8] Yuto Ashida, Zongping Gong, and Masahito Ueda. Non-Hermitian physics. *Adv. Phys.*, 69(3):249–435, July 2020.
- [9] Shunyu Yao and Zhong Wang. Edge states and topological invariants of non-Hermitian systems. *Phys. Rev. Lett.*, 121(8):086803, August 2018.
- [10] Flore K. Kunst, Elisabet Edvardsson, Jan Carl Budich, and Emil J. Bergholtz. Biorthogonal bulk-boundary correspondence in non-Hermitian systems. *Phys. Rev. Lett.*, 121(2):026808, July 2018.
- [11] Ching Hua Lee and Ronny Thomale. Anatomy of skin modes and topology in non-Hermitian systems. *Phys. Rev. B*, 99(20):201103, May 2019.
- [12] Nobuyuki Okuma, Kohei Kawabata, Ken Shiozaki, and Masatoshi Sato. Topological origin of non-Hermitian skin effects. *Phys. Rev. Lett.*, 124(8):086801, February 2020.
- [13] T. Helbig, T. Hofmann, S. Imhof, M. Abdelghany, T. Kiessling, L. W. Molenkamp, C. H. Lee, A. Szameit, M. Greiter, and R. Thomale. Generalized bulk–boundary correspondence in non-Hermitian topoelectrical circuits. *Nat. Phys.*, 16(7):747–750, July 2020.

- [14] Lei Xiao, Tianshu Deng, Kunkun Wang, Gaoyan Zhu, Zhong Wang, Wei Yi, and Peng Xue. Non-Hermitian bulk–boundary correspondence in quantum dynamics. *Nat. Phys.*, 16(7):761–766, July 2020.
- [15] Sebastian Weidemann, Mark Kremer, Tobias Helbig, Tobias Hofmann, Alexander Stegmaier, Martin Greiter, Ronny Thomale, and Alexander Szameit. Topological funneling of light. *Science*, 368(6488):311–314, April 2020.
- [16] Ananya Ghatak, Martin Brandenbourger, Jasper van Wezel, and Corentin Coulais. Observation of non-Hermitian topology and its bulk–edge correspondence in an active mechanical metamaterial. *Proc. Natl. Acad. Sci.*, 117(47):29561–29568, November 2020.
- [17] Kunkun Wang, Tianyu Li, Lei Xiao, Yiwen Han, Wei Yi, and Peng Xue. Detecting non-Bloch topological invariants in quantum dynamics. *Phys. Rev. Lett.*, 127(27):270602, December 2021.
- [18] Emil J. Bergholtz, Jan Carl Budich, and Flore K. Kunst. Exceptional topology of non-Hermitian systems. *Rev. Mod. Phys.*, 93(1):015005, February 2021.
- [19] Kun Ding, Chen Fang, and Guancong Ma. Non-Hermitian topology and exceptional-point geometries. *Nat. Rev. Phys.*, 4(12):745–760, December 2022.
- [20] Xiujuan Zhang, Tian Zhang, Ming-Hui Lu, and Yan-Feng Chen. A review on non-Hermitian skin effect. *Adv. Phys.: X.*, 7(1):2109431, December 2022.
- [21] Nobuyuki Okuma and Masatoshi Sato. Non-Hermitian topological phenomena: A review. *Annu. Rev. Condens. Matter Phys.*, 14(1):83–107, 2023.
- [22] Rijia Lin, Tommy Tai, Linhu Li, and Ching Hua Lee. Topological non-Hermitian skin effect. *Front. Phys.*, 18(5):53605, July 2023.
- [23] Naomichi Hatano and David R. Nelson. Localization transitions in non-Hermitian quantum mechanics. *Phys. Rev. Lett.*, 77(3):570–573, July 1996.
- [24] A. Basiri, Y. Bromberg, A. Yamilov, H. Cao, and T. Kottos. Light localization induced by a random imaginary refractive index. *Phys. Rev. A*, 90(4):043815, October 2014.
- [25] A. F. Tzortzakakis, K. G. Makris, and E. N. Economou. Non-Hermitian disorder in two-dimensional optical lattices. *Phys. Rev. B*, 101(1):014202, January 2020.
- [26] Kohei Kawabata and Shinsei Ryu. Nonunitary scaling theory of non-Hermitian localization. *Phys. Rev. Lett.*, 126(16):166801, April 2021.

- [27] Xunlong Luo, Tomi Ohtsuki, and Ryuichi Shindou. Universality classes of the Anderson transitions driven by non-Hermitian disorder. *Phys. Rev. Lett.*, 126(9):090402, March 2021.
- [28] I. Yusipov, T. Laptyeva, S. Denisov, and M. Ivanchenko. Localization in open quantum systems. *Phys. Rev. Lett.*, 118(7):070402, February 2017.
- [29] Quan Lin, Tianyu Li, Lei Xiao, Kunkun Wang, Wei Yi, and Peng Xue. Observation of non-Hermitian topological Anderson insulator in quantum dynamics. *Nat. Commun.*, 13(1):3229, June 2022.
- [30] Sebastian Weidemann, Mark Kremer, Stefano Longhi, and Alexander Szameit. Coexistence of dynamical delocalization and spectral localization through stochastic dissipation. *Nat. Photon.*, 15(8):576–581, August 2021.
- [31] A. F. Tzortzakakis, K. G. Makris, A. Szameit, and E. N. Economou. Transport and spectral features in non-Hermitian open systems. *Phys. Rev. Res.*, 3(1):013208, March 2021.
- [32] A. Leventis, K. G. Makris, and E. N. Economou. Non-Hermitian jumps in disordered lattices. *Phys. Rev. B*, 106(6):064205, August 2022.
- [33] Stefano Longhi. Anderson localization in dissipative lattices. *Ann. Phys.*, 535(5):2200658, 2023.
- [34] Bo Li, Chuan Chen, and Zhong Wang. Universal non-Hermitian transport in disordered systems. *Phys. Rev. Lett.*, 135(3):033802, July 2025.
- [35] Stefano Longhi. Erratic non-Hermitian skin localization. *Phys. Rev. Lett.*, 134(19):196302, May 2025.
- [36] Li Zhang, Yihao Yang, Yong Ge, Yi-Jun Guan, Qiaolu Chen, Qinghui Yan, Fujia Chen, Rui Xi, Yuanzhen Li, Ding Jia, Shou-Qi Yuan, Hong-Xiang Sun, Hongsheng Chen, and Baile Zhang. Acoustic non-Hermitian skin effect from twisted winding topology. *Nat. Commun.*, 12(1):6297, November 2021.
- [37] Jing-Jing Liu, Zheng-Wei Li, Ze-Guo Chen, Weiyuan Tang, An Chen, Bin Liang, Guancong Ma, and Jian-Chun Cheng. Experimental realization of Weyl exceptional rings in a synthetic three-dimensional non-Hermitian phononic crystal. *Phys. Rev. Lett.*, 129(8):084301, August 2022.
- [38] Zhao-Xian Chen, Yuan-Hong Zhang, Xiao-Chen Sun, Ruo-Yang Zhang, Jiang-Shan Tang, Xin Yang, Xue-Feng Zhu, and Yan-Qing Lu. Direct measurement of topological invariants through temporal adiabatic evolution of bulk states in the synthetic Brillouin zone. *Phys. Rev. Lett.*, 134(13):136601, April 2025.

- [39] Shuaishuai Tong, Qicheng Zhang, Liangjun Qi, Gaohan Li, Xiling Feng, and Chunyin Qiu. Observation of Floquet-Bloch braids in non-Hermitian spatiotemporal lattices. *Phys. Rev. Lett.*, 134(12):126603, March 2025.
- [40] Jia-Xin Zhong, Pedro Fittipaldi De Castro, Tianhong Lu, Jeewoo Kim, Mourad Oudich, Jun Ji, Li Shi, Kai Chen, Jing Lu, Yun Jing, and Wladimir A. Benalcazar. Higher-order skin effect and its observation in an acoustic kagome lattice. *Phys. Rev. B*, 111(1):014314, January 2025.
- [41] Jia-Xin Zhong, Jeewoo Kim, Kai Chen, Jing Lu, Kun Ding, and Yun Jing. Experimentally probing non-Hermitian spectral transition and eigenstate skewness. *Phys. Rev. B*, 112(22):L220301, December 2025.
- [42] Bikashkali Midya. Topological phase transition in fluctuating imaginary gauge fields. *Phys. Rev. A*, 109(6):L061502, June 2024.
- [43] Erik Sparre Andersen. On the fluctuations of sums of random variables. *Math. Scand.*, 1(2):263–285, 1953.
- [44] Erik Sparre Andersen. On the fluctuations of sums of random variables II. *Math. Scand.*, 2(2):195–223, 1954.
- [45] F. Spitzer. *Principles of Random Walks*. Springer, New York, 1964.
- [46] W. Feller. *An Introduction to Probability Theory and Its Applications*, volume I. John Wiley & Sons, New York, 3rd edition, 1968.

Methods

Details of dynamics theory of ENHSL

Model and evolution equation. We consider the 1D Hatano-Nelson chain with stochastic imaginary gauge field h_n on each link, with hoppings shown in Eq. (1). In the single-particle sector, the dynamical equations for the (non-normalized) probability amplitudes $\psi_n(t)$ satisfy

$$i \frac{d\psi_n}{dt} = J_n^L \psi_{n+1} + J_{n-1}^R \psi_{n-1} = J \left(e^{-h_n} \psi_{n+1} + e^{h_{n-1}} \psi_{n-1} \right), \quad (6)$$

with either OBC ($\psi_0 = \psi_{N+1} = 0$) or PBC ($\psi_{n+N} = \psi_n$). Note that under OBC, boundary effects play no role in wave packet expansion provided the excitation starts in the bulk and the wave packet does not reach the edges within the observation time.

Random-walk landscape and non-unitary gauge transformation. The cumulative gauge field (random-walk landscape) is defined as Eq. (2), which maps the sequence $\{h_n\}$ to a discrete-time symmetric random walk in n . Introduce the non-unitary gauge transformation

$$\psi_n(t) = \phi_n(t) \exp(X_n) \equiv \phi_n(t) u_n, \quad u_n = \exp(X_n). \quad (7)$$

Substituting Eq. (7) into Eq. (6) yields the uniform Hermitian transport equation

$$i \frac{d\phi_n}{dt} = J(\phi_{n+1} + \phi_{n-1}). \quad (8)$$

For a single-site initial excitation at $n = 0$, the Hermitian solution is

$$\phi_n(t) = (-i)^n J_n(2Jt), \quad (9)$$

where $J_n(\cdot)$ is the Bessel function of the first kind. Therefore,

$$|\psi_n(t)|^2 = J_n^2(2Jt) \exp(2X_n) = J_n^2(2Jt) u_n^2. \quad (10)$$

In the experiment we analyze the normalized occupation probability profile

$$P_n(t) = \frac{|\psi_n(t)|^2}{\sum_{n'} |\psi_{n'}(t)|^2} = \frac{J_n^2(2Jt) \exp(2X_n)}{\sum_{n'} J_{n'}^2(2Jt) \exp(2X_{n'})}. \quad (11)$$

Equation (11) makes explicit the central structure. The temporal spreading of the wave packet resembles the standard Hermitian Bessel profile, modulated by the random envelope $u_n^2 = \exp(2X_n)$, which locally amplifies ($X_n > 0$) or suppresses ($X_n < 0$) intensity. The excitation is statistically drawn toward the dominant excursion (local maxima) of X_n within the dynamically

accessible interval, producing strong localization peaks in each realization.

Light-cone bound and unit convention. The Bessel kernel $J_n^2(2Jt)$ decays rapidly, with tails falling faster than exponentially outside the interval $|n| \gtrsim 2Jt$, effectively defining a Lieb-Robinson (LR) bound—or light cone—for nearest-neighbor hopping:

$$|n| \lesssim n_{\text{LB}}(t), \quad n_{\text{LB}}(t) \simeq 2Jt. \quad (12)$$

If the hopping is reported in angular-frequency units (rad/s), Eq. (12) is used directly. If the hopping is reported in Hz (cycles/s), one should convert $J_\omega = 2\pi J_{\text{Hz}}$ and write

$$n_{\text{LB}}(t) \simeq 2J_\omega t = 2(2\pi J_{\text{Hz}}) t. \quad (13)$$

In this work, all hoppings and onsite potentials are reported in Hz, so Eq. (13) is used.

Second-moment spreading observable. The evolution of the wave packet's spatial spread in a single-realization of disorder is quantified using the second moment:

$$d(t) = \sqrt{\sum_n n^2 P_n(t)} = \sqrt{\frac{\sum_n n^2 J_n^2(2Jt) \exp(2X_n)}{\sum_n J_n^2(2Jt) \exp(2X_n)}}. \quad (14)$$

In the disorder-free limit $h_n = 0$ (hence $X_n = 0$), one recovers ballistic spreading $d(t) = \sqrt{2} Jt$.

Lévy-arc sine law for dominant-site distribution. Let $u_n = \exp(X_n)$ and consider the thermodynamic limit $N \rightarrow \infty$. From the central limit theorem, for large n one has

$$\frac{1}{\sqrt{2n}} \log \left| \frac{u_n}{u_0} \right| \sim \mathcal{N}(0, \Delta h^2), \quad (15)$$

where $\mathcal{N}(0, \Delta h^2)$ is the normal distribution with zero mean and variance Δh^2 , so that typical envelope amplitudes behave as

$$u_n \sim \exp(-\Delta h \sqrt{n}), \quad (16)$$

showing a sub-exponential but stronger-than-algebraic decay [35].

For finite time t , the Bessel profile $J_n^2(2Jt)$ is confined within the light cone $|n| < n_{\text{LB}}(t) = 2Jt$, with rapid decay outside. Thus $|\psi_n(t)|^2$ is predominantly localized around the site $n = n_0(t)$ where X_n attains its maximum within $(-n_{\text{LB}}(t), n_{\text{LB}}(t))$:

$$n_0(t) = \arg \max_{-n_{\text{LB}} < n < n_{\text{LB}}} X_n. \quad (17)$$

Here n_0 is a random variable with a universal limiting distribution for large t , which follows from the Sparre-Andersen theorem [43–46]. This theorem states that many fluctuation properties

of symmetric random walks do not depend on the actual distribution $f(h)$, provided that increments are continuous and the distribution is symmetric about $h = 0$. Assuming that the random walk has independent and identically distributed symmetric $\pm h$ increments, the probability distribution can be calculated using standard ballot/reflection arguments [45, 46] and reads

$$P(n_0 = n, t) = \frac{\binom{2(n+n_{\text{LB}})}{n+n_{\text{LB}}} \binom{2(n_{\text{LB}}-n)}{n_{\text{LB}}-n}}{\binom{4n_{\text{LB}}}{2n_{\text{LB}}}}, \quad n = -n_{\text{LB}} + 1, \dots, n_{\text{LB}} - 1, \quad (18)$$

with $n_{\text{LB}}(t) = 2Jt$. Using Stirling's approximation,

$$\binom{2n}{n} \sim \frac{4^n}{\sqrt{\pi n}}, \quad (19)$$

for large n , this reduces to

$$P_{\text{arc}}(n_0 = n, t) \sim \sqrt{\frac{n_{\text{LB}}}{\pi(n - n_{\text{LB}})(n + n_{\text{LB}})}}. \quad (20)$$

The resulting distribution of n_0 is the universal arcsin Lévy law, which indicates an enhanced probability of finding n_0 , and thus localization of excitation, near the light-cone edges $n \rightarrow \pm n_{\text{LB}} = \pm 2Jt$.

Second moment averaged over disorder realizations. An approximate expression of the second moment averaged over all locations can be computed as

$$\langle d(t) \rangle = \sqrt{\sum_{n=-n_{\text{LB}}}^{n_{\text{LB}}} n^2 P_{\text{arc}}(n_0 = n, t)}. \quad (21)$$

By setting $n = xn_{\text{LB}}$ with $x \in [-1, 1]$ and using Eq. (20), in the limit $n_{\text{LB}} \rightarrow \infty$ one has

$$\langle d(t) \rangle = n_{\text{LB}} \sqrt{\int_{-1}^1 x^2 P_0(x) dx} = \sqrt{2} Jt, \quad (22)$$

where $P_0(x) = \frac{1}{\pi\sqrt{1-x^2}}$ is the standard arcsine distribution on $[-1, 1]$, and the second moment of $P_0(x)$ is known to be $1/2$. Equation (22) clearly shows the ballistic scaling of the disorder-averaged second moment. In our experiments, the accessible sites extend to $|n| \sim 30$, for which the Stirling-based asymptotic approximation Eq. (19) is already accurate at the percent level.

Implementation of non-Hermitian acoustic lattices

The non-Hermitian acoustic lattices consists of multiple 3D-printed acoustic cavities (see Supplementary Materials for dimensions), each representing a site in the non-Hermitian lattice

and operating near its first dipole resonance around 1040 Hz. The tuning of onsite potentials and hoppings is implemented using active components, specifically loudspeaker-microphone (pump-probe) pairs, an audio amplifier (LM386), and an phase shifter integrated in a customized controller (see Supplementary Materials for details). The loudspeaker and microphone are positioned at the bottom of each cavity. The microphone captures the acoustic pressure signal, which is processed by the amplifier and phase shifter to adjust its amplitude and phase before being emitted by the loudspeaker in the connected cavity (see [41] for details).

The imaginary gauge disorder is implemented by implementing an asymmetry between the right and left hopping magnitudes according to Eq. (1), i.e., $J_n^R/J_n^L = \exp(2h_n)$, while keeping the geometric mean fixed at J . Global reciprocity is enforced by choosing sequences $\{h_n\}$ satisfying $\sum_n h_n = 0$. In practice, the values are calibrated by independent measurements of the effective hoppings (e.g., via two-site characterization, see [41]).

Spectral reconstruction via Green's function measurements

For a chain of N sites, we measure the steady-state complex response at all probe sites i for each pump site j under monochromatic excitation at frequency ω . This yields the full response matrix $G_{ij}(\omega)$ over a discrete set of drive frequencies spanning the band of interest. The magnitude and phase are obtained by referencing the microphone signals to the excitation signal, allowing coherent extraction of $G_{ij}(\omega)$. The full matrix acquisition over all pump-probe pairs yields N^2 complex transfer functions per frequency point [41].

In the effective tight-binding description, the Green's function satisfies

$$G(\omega) = (\omega - H)^{-1}, \quad (23)$$

so the eigenvectors of $G(\omega)$ coincide with those of H , and its eigenvalues follow the single-pole form

$$\lambda_m(\omega) = \frac{1}{\omega - E_m}. \quad (24)$$

up to a complex prefactor set by the measurement normalization. We therefore diagonalize $G(\omega)$ for each sampled ω , track each eigenvalue branch $\lambda_m(\omega)$ across frequency, and fit to Eq. (24) to extract E_m . This procedure yields both $\text{Re}(E_m)$ and $\text{Im}(E_m)$, allowing direct access to the complex spectrum. Eigenmodes are obtained from the corresponding eigenvectors of $G(\omega)$ evaluated near $\omega \simeq \text{Re}(E_m)$, where the response is dominated by the target pole. If needed, left eigenvectors can be obtained analogously from the left eigen-decomposition of $G(\omega)$; in the present work, we focus on the mode amplitudes and IPR used in Fig. 3.

Time-resolved propagation measurements

Time-domain dynamics are initiated by driving the central site ($n = 0$) with a Gaussian-modulated tone burst, Eq. (3). The carrier frequency is set to $\text{Re}(\omega_0) = 1040$ Hz (near the band center), and the envelope width is chosen as $\sigma = 10$ ms following the criteria discussed in the main text (Fig. 2d–f). The driving signal is generated by a multi-channel data-acquisition card (PCIe-6353, National Instruments) and applied to the on-site loudspeaker (CMS-15118D-L100, CUI Devices) through an audio amplifier (LM386, Texas Instruments). The time-domain waveform at each site is recorded simultaneously using MEMS microphones (BOB-19389, SparkFun Electronics) at a sampling rate of 16 kHz, with all channels acquired synchronously.

The recorded pressure signals are digitally bandpass-filtered around the carrier frequency (1010–1070 Hz). The envelope of the signal is taken as $|\psi_n(t)|$. At each time t , we normalize $\psi_n(t)$ by its instantaneous norm, so that $\sum_n |\psi_n(t)|^2 = 1$ for all t .

To obtain ensemble statistics, we repeat the measurement for R disorder realizations and evaluate $n_0^{(r)}(t)$ at a fixed evolution time t (chosen as large as permitted by avoiding boundary reflections). The empirical distribution is

$$\hat{P}(n_0, t) = \frac{1}{R} \sum_{r=1}^R \delta_{n_0, n_0^{(r)}(t)}, \quad (25)$$

where $\delta_{i,j}$ is the Kronecker delta. For visualization from a finite ensemble, we further smooth $\hat{P}(n_0, t)$ using a bounded, boundary-corrected Gaussian kernel density estimator on the finite support $n_0 \in (-n_{\text{LB}}(t), n_{\text{LB}}(t))$, in which the Gaussian kernel centered at each sample is truncated to the interval and renormalized to remove boundary bias; the bandwidth is selected via leave-one-out likelihood cross-validation.

Figures

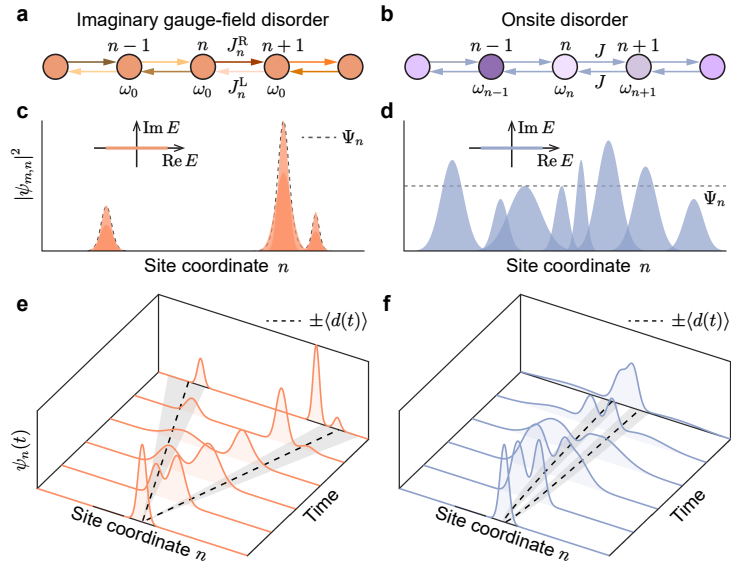


Figure 1: Conceptual comparison between ENHSL and Hermitian Anderson localization. **a**, Tight-binding schematic of a globally reciprocal non-Hermitian chain with disordered imaginary gauge fields (hopping disorder). Sites share a uniform onsite potential (ω_0), while the link colors indicate spatially fluctuating non-reciprocal hoppings ($J_n^{L/R}$). **b**, Hermitian Anderson chain with onsite disorder (site colors, ω_n) and Hermitian uniform hoppings (J). **c**, Spectral signatures of ENHSL. The inset sketches the complex spectrum, which remains (approximately) real despite non-reciprocal hoppings under global reciprocity. The main panel illustrates a typical ENHSL eigenstate profile featuring a dominant bulk peak accompanied by two weaker satellite peaks; the dashed curve indicates the summed eigenstate intensity $\Psi_n = \sum_m |\psi_{m,n}|^2$, which is dominated by the same peak structure. **d**, Spectral signatures of Anderson localization: many exponentially localized eigenstates centered at different sites, yielding a relatively featureless mode-summed profile Ψ_n (dashed line). **e**, Dynamical response in ENHSL following a bulk-centered excitation. The 3D traces show the spatiotemporal evolution of the wave-packet envelope $\psi_n(t)$ for a single disorder realization. Dashed guidelines show the symmetric ensemble-averaged spreading envelope, $n = \pm\langle d(t) \rangle$ (gray shading: realization-to-realization fluctuations), highlighting the ballistic transport. **f**, Dynamical response in the Anderson case, where the wave packet remains dynamically localized and the ensemble-averaged spreading saturates at long times (dashed guideline).

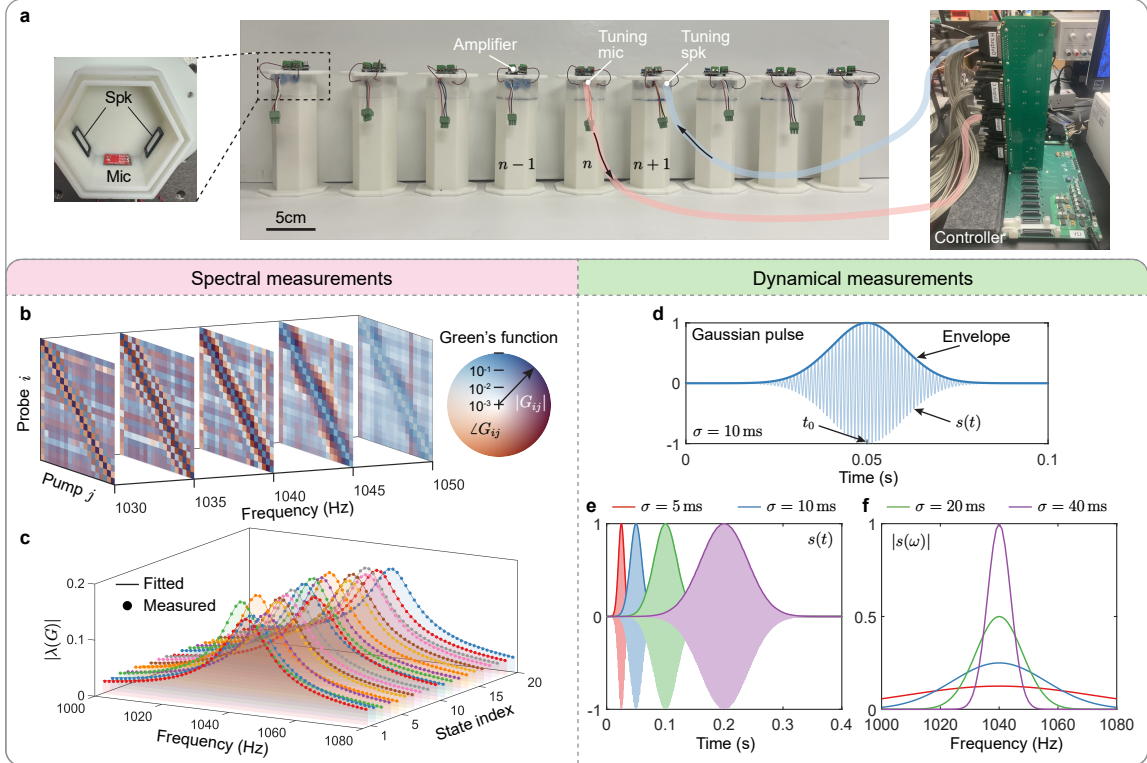


Figure 2: Unified spectral-and-dynamical measurement protocol on the same acoustic lattice. **a**, Photograph of the experimental platform: a 1D chain of acoustic resonators (interior view shown at left, containing a microphone and two loudspeakers) coupled by electroacoustic feedback implemented with external amplifiers and phase shifters integrated in a multi-channel controller (right). Here, a representative hopping from site n to site $n + 1$ is illustrated. **b,c**, Green's-function-based spectroscopy for full spectral reconstruction. **b**, Site-by-site excitation (pump j) together with full spatial readout (probe i) yields the frequency-resolved response (Green's-function) matrix $G_{ij}(\omega)$. Shown is an example lattice of size $N = 20$ under OBC ($\omega_0 = 1040 \text{ Hz} - 6i \text{ Hz}$, $J = 1.5 \text{ Hz}$, $\Delta h = 2 \text{ Hz}$), with $G_{ij}(\omega)$ visualized at several representative frequencies. The inset color wheel indicates the visualization scheme: hue encodes the phase $\angle G_{ij}$, while brightness encodes the magnitude $|G_{ij}|$ (log-scaled). **c**, Extraction of complex eigenenergies from the measured Green's function. Dots show the measured magnitudes of the eigenvalues $\lambda_m(\omega)$ of $G(\omega)$ as functions of frequency, and solid curves show fits to a single-pole form $\lambda_m(\omega) \simeq A_m/(\omega - E_m)$, from which the complex eigenenergies E_m are obtained. **d–f**, Time-resolved wave-packet measurements using the same lattice. **d**, Gaussian-modulated tone burst $s(t)$ centered at $\text{Re}(\omega_0) = 1040 \text{ Hz}$, illustrating the carrier and the Gaussian envelope (width σ) with temporal center $t_0 = 5\sigma$. **e,f**, Excitation waveforms $s(t)$ (e) and their spectra $|s(\omega)|$ (f) for four representative envelope widths $\sigma = 5, 10, 20$, and 40 ms .

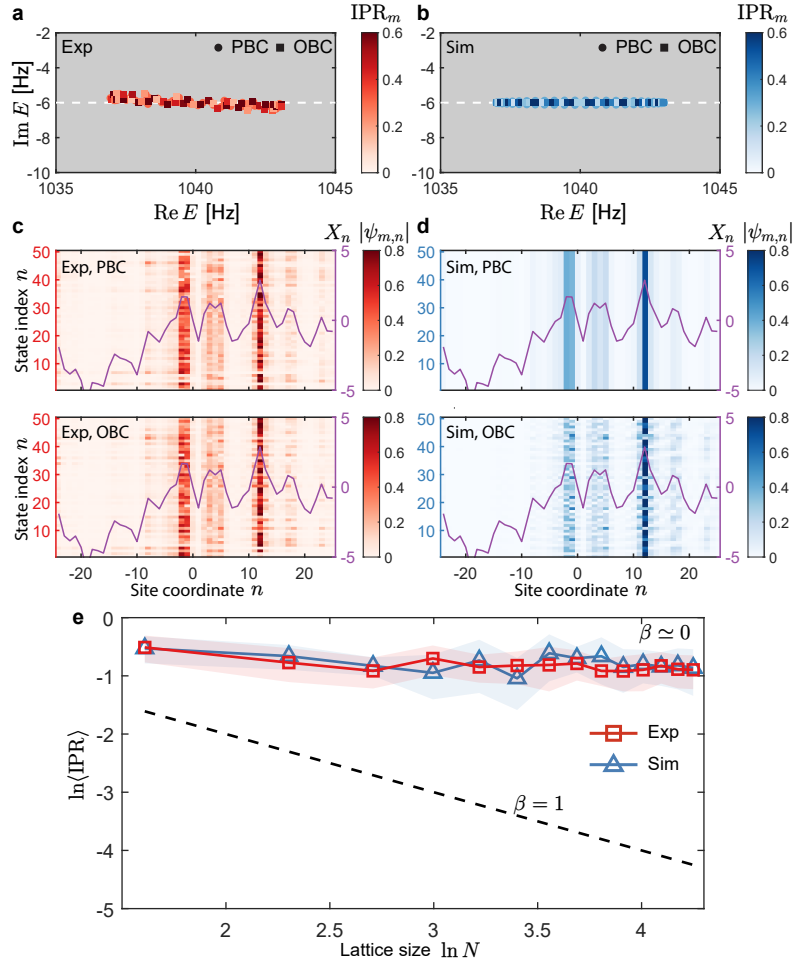


Figure 3: Spectral signatures of ENHSL, comparing experiments and tight-binding simulations for a chain of size $N = 50$ with $\omega_0 = 1040$ Hz – $6i$ Hz, $J = 1.5$ Hz, and $\Delta h = 2$ Hz. **a,b**, Complex spectra for a representative realization under both PBC and OBC. Circles (squares) denote PBC (OBC) energies, and colors encode IPR_m . The dashed horizontal line marks the nominal uniform background-loss level (-6 Hz) used as a reference. **c,d**, Spatial distributions of all eigenstates under PBC (top) and OBC (bottom) for experiment (c) and simulation (d). Heat maps show the eigenstate amplitudes $|\psi_{m,n}|$ as functions of eigenstate index m and site coordinate n . The overlaid purple curve (right axis) shows the random-walk landscape X_n associated with the imaginary-gauge-field disorder, highlighting that prominent localization peaks occur near large excursions of X_n . **e**, Scaling of localization with system size under OBC. Symbols show the ensemble-averaged $\langle IPR \rangle$ for $N = 5, 10, 15, \dots, 70$ (each N averaged over $R = 8$ disorder realizations), comparing experiment and simulation; shaded bands indicate the realization-to-realization spread (standard deviation). The dashed guideline ($\beta = 1$) indicates the extended-state scaling $IPR \propto N^{-1}$. A fit to $\langle IPR \rangle \propto N^{-\beta}$ yields $\beta \simeq 0$, consistent with size-independent localization in ENHSL.

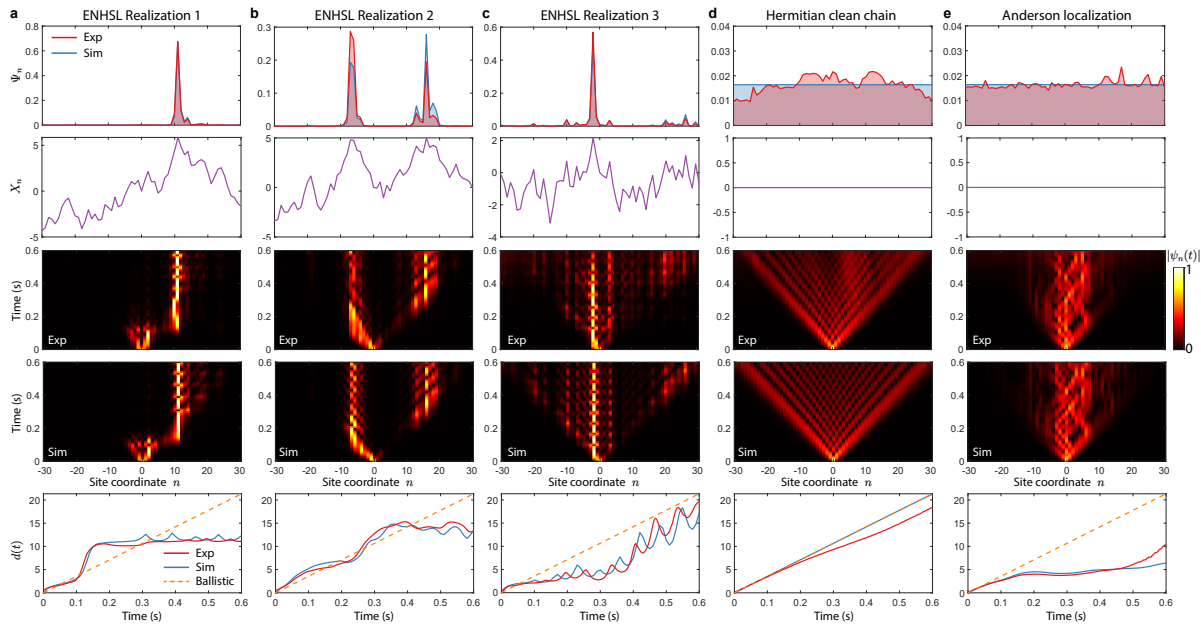


Figure 4: Experimental observation of wave-packet propagation following excitation at the central site ($n = 0$) in a chain of length $N = 61$ under OBC. The parameters set in experiments are $\omega_0 = 1040 \text{ Hz} - 1.75i \text{ Hz}$, $J = 4 \text{ Hz}$, and $\Delta h = 1.6 \text{ Hz}$. **a,b,c**, Three representative disorder realizations of the ENHSL. **d**, Disorder-free Hermitian chain (clean reference). **e**, Hermitian chain with onsite disorder showing Anderson localization (reference). For each panel, rows from top to bottom show: (i) the spatial profile of the eigenstate intensity summed over all states, $\Psi_n = \sum_m |\psi_{m,n}|^2$; (ii) the random-walk landscape X_n ; (iii) the experimentally measured spatiotemporal evolution of the acoustic pressure envelope $|\psi_n(t)|$; (iv) the corresponding tight-binding simulation; and (v) the spreading distance $d(t)$ extracted from experiment (blue solid) and simulation (red solid), with the ballistic law shown for comparison (orange dashed).

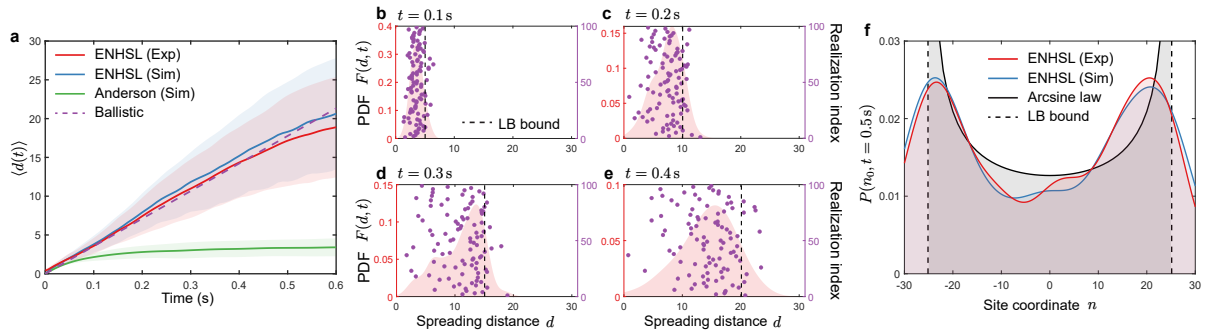


Figure 5: Ensemble statistics of wave-packet spreading for the ENHSL (OBC, $N = 61$), obtained from $R = 100$ disorder realizations. The parameters set in experiments are $\omega_0 = 1040$ Hz – $1.75i$ Hz, $J = 4$ Hz, and $\Delta h = 1.6$ Hz. **a**, Ensemble-averaged spreading distance $\langle d(t) \rangle$ from experiments and tight-binding simulations, compared with the ballistic scaling of a clean Hermitian chain and with a Hermitian Anderson-localized reference (shown by simulations, exhibiting saturation). **b–e**, Distributions of the spreading distance at fixed times $t = 0.1, 0.2, 0.3$, and 0.4 s, respectively. In each panel, purple markers indicate the values $d^{(r)}(t)$ from individual realizations r (realization index shown on the right axis). The shaded curves show the probability density function (PDF) $F(d, t)$ (left axis) estimated from the finite ensemble using a bounded KDE method on the interval $(0, 30)$. The dashed lines denote the Lieb-Robinson (LB) bound, $n_{\text{LB}}(t) = 2Jt$. **f**, PDF of the dominant propagation site, $n_0(t) = \arg \max_n |\psi_n(t)|$, at $t = 0.5$ s, obtained from the same $R = 100$ realizations, and estimated using a bounded KDE method on the interval $(-30, 30)$. Experimental and simulated distributions are compared. The dashed vertical lines indicate the corresponding LB bounds, $\pm n_{\text{LB}}$, and the black curve shows the Lévy arcsine-law prediction restricted to the interval $(-n_{\text{LB}}, n_{\text{LB}})$.